





29

## Abstract

30 Sudden wind direction and speed shifts from outflow boundaries (OFBs) associated with deep  
31 convection significantly affect weather in the lower troposphere. Specific OFB impacts include  
32 rapid variation in wildfire spread rate and direction, the formation of convection, aviation hazards,  
33 and degradation of visibility and air quality due to mineral dust aerosol lofting. Despite their  
34 recognized importance to operational weather forecasters, OFB characterization (location, timing,  
35 intensity, etc.) in numerical models remains challenging. Thus, there remains a need for objective  
36 OFB identification algorithms to assist decision support services. With two operational next-  
37 generation geostationary satellites now providing coverage over North America, high-temporal  
38 and spatial resolution satellite imagery provides a unique resource for OFB identification. A  
39 system is conceptualized here designed around the new capabilities to objectively derive dense  
40 mesoscale motion flow fields in the Geostationary Operational Environmental Satellite (GOES)-  
41 16 imagery via optical flow. OFBs are identified here by isolating linear features in satellite  
42 imagery, and back-tracking them using optical flow to determine if they originated from a deep  
43 convection source. This “objective OFB identification” is tested with a case study of an OFB  
44 triggered dust storm over southern Arizona. Results highlight the importance of motion  
45 discontinuity preservation, revealing that standard optical flow algorithms used with previous  
46 studies underestimate wind speeds when background pixels are included in the computation with  
47 cloud targets. The primary source of false alarms is incorrect identification of line-like features in  
48 the initial satellite imagery. Future improvements to this process are described to ultimately  
49 provide a fully automated OFB identification algorithm.



## 50 1. Introduction

51 Downburst outflows from associated deep convection (Byers and Braham Jr., 1949; Mitchell  
52 and Hovermale, 1977) play a significant, dynamic role in modulation of the lower troposphere.  
53 Their direct impacts to society are readily apparent—capsizing boats on lakes and rivers with  
54 winds that seem to “*come out of nowhere*” (e.g. The Branson, MO duck boat accident; Associated  
55 Press 2018), causing shifts in wildfire motion and fire intensity that put firefighters in harm’s way  
56 (e.g. the Waldo Canyon and Yarnell Hill Fires; Hardy and Comfort, 2015; Johnson et al., 2014),  
57 and threatening aviation safety at regional airports with sudden shifts from head to tail-winds and  
58 turbulent wakes (Klinge et al., 1987; Uyeda and Zrnić, 1986). In the desert southwest, convective  
59 outflows can loft immense amounts of dust, significantly reducing surface visibility and air quality  
60 for those within the impacted area (e.g. Idso et al. 1972; Raman et al. 2014). These outflows are  
61 commonly associated with rapid temperature, pressure, and moisture changes at the surface  
62 (Mahoney III, 1988). Furthermore, the collision of outflows from adjacent storms can serve as the  
63 focal point of incipient convection or the intensification of nascent storms (Rotunno et al., 1988;  
64 Mueller et al., 2003).

65 Despite the understood importance of deep convection and convectively driven outflows, high  
66 resolution models struggle to characterize and identify them (e.g. Yin et al. 2005). At present,  
67 outflow boundaries (OFBs) are instead most effectively monitored in real-time at operational  
68 centers around the world with surface, radar, and satellite data. Satellites often offer the only form  
69 of observation in remote locations. The most common method for detecting outflows via satellite  
70 data involves the identification of clouds formed by strong convergence at the OFB leading edge.  
71 When the lower troposphere is dry, OFBs may be demarcated by an airborne “dust front”, after  
72 passing over certain surfaces prone to deflation by frictional winds (Miller et al., 2008). The task



73 of identifying OFBs can prove quite challenging and would benefit greatly from an objective  
74 means of feature identification and tracking for better decision support services.

75 The Advanced Baseline Imager (ABI), an imaging radiometer carried on board the  
76 Geostationary Operational Environmental Satellite (GOES)-R era systems, offers a leap forward  
77 in capabilities for the real-time monitoring and characterization of OFBs. Its markedly improved  
78 spatial (0.5 vs. 1.0 km visible, 2 km vs. 4 km infrared), spectral (16 vs. 5 spectral bands), and  
79 temporal (5 min vs. 30 min continental U.S., and 15 min vs. 3 hr full disk) resolution provides new  
80 opportunities for passive sampling of the atmosphere over the previous generation (Schmit et al.,  
81 2016). The vast improvement of temporal resolution alone (which includes mesoscale sectors that  
82 refresh as high as 30 s) allows for dramatically improved tracking of convection (Cintineo et al.,  
83 2014; Mecikalski et al., 2016; Sieglaff et al., 2013), fires and pyroconvection (Peterson et al., 2015,  
84 2017, 2018), ice flows, and synoptic scale patterns (Line et al., 2016). This higher temporal  
85 resolution makes identification of features like OFBs easier as well because of greater frame-to-  
86 frame consistency.

87 The goal of this work is to use ABI information towards objective identification of OFBs. One  
88 of the notable challenges in satellite identification of OFBs over radar or models is the lack of  
89 auxiliary information. When working with a radar or a numerical model framework, for example,  
90 additional information is available on the flow, temperature, and pressure tendency of the  
91 boundary. Without that information, however, forecasters must rely on their knowledge of gust  
92 front dynamics to identify OFBs in satellite imagery. Here, we introduce the concept of objectively  
93 derived motion using GOES-16 ABI imagery for feature identification via an advanced optical  
94 flow method, customized to the problem at hand. A case study of a convectively triggered OFB  
95 and accompanying haboob dust front is presented in 5-min GOES-16 contiguous United States



96 (CONUS) sector information, as a way of evaluating and illustrating the potential of the  
97 framework.

98 This paper is outlined as follows. The background for objective motion extraction and OFB  
99 identification is presented in Section 2. The optical flow methods developed for this purpose are  
100 discussed in Section 3. Section 4 presents the case study test of the current algorithm, and Section  
101 5 concludes the paper with a discussion on plans for future work in objective feature identification  
102 from next-generation geostationary imagers of similar fidelity to the GOES-R ABI, which are  
103 presently coming online around the globe.

104

105 **2. Background**

106 *2.1 Previous Work in OFB Detection*

107 Objective identification of OFBs in meteorological data has been a topic of scientific inquiry  
108 for more than 30 years. Uyeda and Zrnić (1986) and Hermes et al. (1993) use detections of wind  
109 shifts in terminal Doppler radar velocity measurements to isolate regions of strong radial shear  
110 associated with OFBs. Smalley et al. (2007) include the “fine line” reflectivity structure of  
111 biological- and precipitation-sized particles to identify OFBs via image template matching.  
112 Chipilski et al. (2018) considered the OFB objective identification in numerical models using  
113 similar image processing techniques, but with additional dynamical constraints on vertical velocity  
114 magnitudes and mean-sea level pressure tendency. Objective OFB identification has not been  
115 demonstrated to date with the new ABI observations of the GOES-R satellite series. Identification  
116 via satellite imagery would be valuable for local deep convection nowcasting algorithms which  
117 use boundary presence as a predictor field (Mueller et al., 2003; Roberts et al., 2012), and for



118 operational centers around the world which may not have access to ground-based Doppler radar  
119 data.

120 Traditionally, forecasters have identified OFBs in satellite imagery by visually identifying  
121 quasi-linear low-level cloud features and back-tracking them to an associated deep convection  
122 source. Previous objective motion derivation algorithms are not designed to yield the dense wind  
123 fields necessary for identifying and tracking features such as OFBs (Bedka et al., 2009; Velden et  
124 al., 2005). In fact, the original image window-matching atmospheric motion vector (AMV)  
125 algorithms produce winds only over targets deemed acceptable for tracking by pre-processing  
126 checks on the number of cloud layers in a scene, brightness gradient strength, and patch coherency.  
127 The targets are further filtered with post-processing checks on acceleration and curvature through  
128 three-frame motion and deviation from numerical model flow (Bresky et al., 2012; Nieman et al.,  
129 1997; Velden et al., 1997). These practices were followed for a very practical reason—AMV  
130 algorithms were tailored for model data assimilation. In the formation of the model analysis,  
131 observational data must be heavily quality-controlled with outliers removed, to minimize data  
132 rejection. Here, information such as OFBs would be rejected due to the detailed space/time  
133 structure of actual convection which is typically poorly represented by the numerical model.

134 Deriving two-dimensional flow information at every point in the imagery would require either  
135 modification of previous AMV schemes or post-processing of the AMV data via objective analysis  
136 (e.g. Apke et al. 2018). The latter typically will not capture motion field discontinuities, resulting  
137 in incorrect flows near feature edges (Apke et al., 2016). To capture such discontinuities in a dense  
138 flow algorithm, new computer vision techniques, such as the gradient-based methods of optical  
139 flow, must be adopted.



140 2.2 Optical Flow Techniques

141 Optical flow gradient-based techniques derive motion within fixed windows, thus eliminating  
142 the reliance on models for defining a search region. A core assumption of many optical flow  
143 techniques is brightness constancy (Horn and Schunck, 1981). Considering two image frames,  
144 brightness constancy states that the image intensity  $I$  at some point  $\mathbf{x} = [x, y]^T$  is equal to the  
145 image intensity in the subsequent frame at a new point,  $\mathbf{x} + \mathbf{U}$ , where  $\mathbf{U} = [u, v]^T$  represents the  
146 flow components of the image over the time interval ( $\Delta t$ ) between the two images:

$$I(\mathbf{x}, t) = I(\mathbf{x} + \mathbf{U}, t + \Delta t) \quad (1)$$

147 Eq. (1) can be linearized to solve for the individual flow components,  $u$  and  $v$ :

$$\nabla I \cdot \mathbf{U} + I_t = 0 \quad (2)$$

148 Where  $\nabla I = [I_x, I_y]$  represents the intensity gradients in the x and y direction, and  $I_t$  represents  
149 the temporal gradient of intensity. For one image pixel, Eq. (2) contains two unknowns with a  
150 simple translation model for  $\mathbf{U}$ ; therefore, it cannot be solved point-wise. One well-known  
151 approach to solving this so-called “aperture problem” is the Lucas-Kanade, hereafter LK method,  
152 which considers a measurement neighborhood of the intensity space and time gradients (e.g.,  
153 Baker and Matthews, 2004; Bresky and Daniels, 2006). Use of neighborhoods, or image windows,  
154 to derive optical flow are called *local* approaches. Another seminal approach was introduced by  
155 Horn and Schunck (1981; HS Method) which solves the aperture problem by adding an additional  
156 smoothness constraint to the brightness constancy assumption, and minimizing an energy  
157 magnitude between two images:

$$E(u, v) = \iint_{\Omega} (\nabla I \cdot \mathbf{U} + I_t)^2 + \alpha(|\nabla_2 u|^2 + |\nabla_2 v|^2) \, d\mathbf{x} \quad (3)$$



158 Where  $E(u, v)$  represents an energy functional to be minimized over all image pixels  $\Omega$ ,  $\alpha$  is a  
159 constant weight used to control the smoothness of the flow components  $u(\mathbf{x})$  and  $v(\mathbf{x})$ , and  $\nabla_2 =$   
160  $[\partial/\partial x, \partial/\partial y]^T$ . This optical flow derivation is called a *global* approach. Eq. (3) is minimized in  
161 Horn and Schunck (1981) by deriving the Euler-Lagrange equations, and numerically solving with  
162 Gauss-Seidel iterations.

163 Linearizing the brightness constancy equation into Eq. (2) means that large and non-linear  
164 displacements (typically  $> 1$  pixel between images) will not be captured (Brox et al., 2004). Thus,  
165 most optical flow computations initially spatially subsample images to where all displacements  
166 are initially less than 1-pixel (Anandan, 1989; discussed more in Section 3.1), which can cause  
167 fast moving small features to be lost. Note that reducing the temporal resolution of GOES imagery  
168 (e.g. 10-min vs. 5-min scans) increases the displacement of typical meteorological features  
169 between frames. Furthermore, constancy assumptions are more likely violated with reduced  
170 temporal resolution since image intensity changes more through evaporation and condensation of  
171 cloud matter over time. Thus, for the spatial resolution of ABI, it is impractical to consider optical  
172 flow gradient-based methods at temporal resolutions coarser than 5-min for several mesoscale  
173 meteorological phenomena, including OFBs. Very spatially coarse images do not need to be  
174 initially used with faster scanning rates, such as super rapid scan 1-min information (Schmit et al.,  
175 2013), or the 30-s temporal resolution mesoscale mode of ABI (Schmit et al., 2016).

176 While both the LK and HS methods are designed for deriving dense flow in satellite imagery,  
177 neither account for motion discontinuities in fields. Hence, both suffer from incorrect flow  
178 derivations near cloud edges, and would perform poorly for OFB detection and tracking. Black  
179 and Anandan (1996) offer an intuitive solution to this problem, whereby the energy functional is  
180 designed to minimize robust functions that are not sensitive to outliers:



$$E(u, v) = \iint_{\Omega} \rho_d(\nabla I \cdot \mathbf{U} + I_t) + \rho_s(|\nabla_2 u|^2 + |\nabla_2 v|^2) d\mathbf{x} \quad (4)$$

181 The robust function data term for the standard HS approach is simply  $\rho_d(r) = r^2$ , and smoothness  
182  $\rho_s(r) = r$  which implies that energy functionals increase quadratically for  $r$  outliers. Other robust  
183 functions can also be minimized with similar gradient descent algorithms to Gauss-Seidel  
184 iterations, while being less sensitive to outliers (Press et al., 1992; Black and Anandan, 1996).  
185 Robust functions are popular in recent optical flow work (Brox et al., 2004; Sun et al., 2010), and  
186 a similar approach was adopted here and is discussed further in the methodology section. The  
187 reader is referred to works by Barron et al. (1994), Fleet and Weiss (2005), and Sun et al. (2010)  
188 for a more comprehensive review on optical flow techniques.

189 The relevance of optical flow in satellite meteorological research continues to increase now  
190 that scanning rates of sensors such as the ABI are routinely at sub 5-min time scales, making  
191 motion easier to derive objectively (Bresky and Daniels, 2006; Héas et al., 2007; Wu et al., 2016).  
192 The dense motion estimation within fine-temporal resolution data has yet to be used for feature  
193 identification. Optimizing optical flow for this purpose, and its specific application to OFBs, is the  
194 aim of this study. The next section outlines our approach to this end.

195

196 **3. Methodology**

197 *3.1 Optical Flow Approach*

198 A recent approach to handle piecewise and non-linear image changes in flow is introduced by  
199 Brox et al. (2004) (Hereafter B04), where the brightness constancy assumption is no longer  
200 linearized, i.e.



$$\begin{aligned}
 E(u, v) = & \iint_{\Omega} \rho_d(|I(\mathbf{x} + \mathbf{U}, t + \Delta t) - I(\mathbf{x}, t)|^2 \\
 & + \gamma |\nabla_2 I(\mathbf{x} + \mathbf{U}, t + \Delta t) - \nabla_2 I(\mathbf{x}, t)|^2) \\
 & + \alpha \rho_s(|\nabla_2 u|^2 + |\nabla_2 v|^2) d\mathbf{x}
 \end{aligned} \tag{5}$$

201 Following B04, within the data robust function, we now have also included a gradient constancy  
 202 assumption, which is weighted by a constant  $\gamma$  to make the derived flow more resilient to changes  
 203 in illumination. Avoiding linearization of constancy assumptions improves the identification of  
 204 large displacements between images. The Charbonnier penalty is used for the data and smoothness  
 205 robust functions following Sun et al. (2010),

$$\rho_d(r^2) = \rho_s(r^2) = \sqrt{r^2 + \epsilon^2} \tag{6}$$

206 with  $\epsilon$  representing a small constant present to prevent division by zero in minimization, set to  
 207 0.001. The values for  $\mathbf{U}$  are found by solving the Euler-Lagrange equations of Eq. (5) with  
 208 numerical methods

$$E_u - \frac{dE_{u_x}}{dx} - \frac{dE_{u_y}}{dy} = 0 \tag{7}$$

$$E_v - \frac{dE_{v_x}}{dx} - \frac{dE_{v_y}}{dy} = 0 \tag{8}$$

209 with reflecting boundary conditions and subscripts that imply the derivatives. Eqs. (7) and (8) are  
 210 solved with a nested-fixed point successive over-relaxation iteration scheme described in B04 and  
 211 summarized in Fig. 1. The reader is referred to Chapter 4 of Brox (2005) for details on the full  
 212 discretization of the derivatives in the successive over-relaxation scheme. Here, only the spatial  
 213 dimensions are used for the smoothing term, though it is possible to include the time dimension  
 214 with this system as well.



215 A difficulty in solving Eqs. (7) and (8) is that the successive over-relaxation scheme may  
216 converge on a local minimum of  $E(u, v)$ , rather than finding the global minimum. The typical  
217 approach to find the global minimum is to compute optical flow with coarse- to fine-scale warping  
218 iterations (e.g. Anandan, 1989). Coarse-to fine-scale warping iterations work by subsampling the  
219 initial image at native resolution to a coarser spatial resolution and computing the flow initially at  
220 the coarsest resolution in the image pyramid. The  $U$  results from the coarse image flow are then  
221 used as the first guess field to for the next finest scale on the image pyramid (Fig. 2), and the  
222 second image is warped accordingly. The warping step ensures that estimated displacements at  
223 every step in the image pyramid remain small.

224 The B04 scheme includes coarse-to fine-scale warping iterations at every outer iteration  $k$ .  
225 This means that the first iteration is run on a subsampled image, and the subsampling is reduced  
226 by a scale factor at every  $k$  until the image reaches native resolution at the final  $k = nK$ . Images  
227 at every  $k$  in this subsampling are found using a gaussian image pyramid technique with bicubic  
228 interpolation. The flow values of the image at  $k - 1$  are upscaled accordingly at  $k$  also with  
229 bicubic interpolation (the initial flow guess is  $u = v = 0$  at  $k = 0$ ). For improved computation of  
230 spatial derivatives, the initial image is also smoothed with a 9x9 pixel kernel gaussian filter with a  
231 standard deviation set to 1.5 pixels. The specific settings used for the coarse- to fine- warped flow  
232 scheme here are shown in Table 1.

233 *3.2 Objective OFB identification*

234 There are two steps to the objective OFB identification process. First, a linear feature or sharp  
235 boundary is identified in visible or infrared imagery. In some cases, the first step alone is enough  
236 to identify OFBs subjectively. The second step is tracking that feature back in time to see where  
237 it originated from (typically, near an area with deep convection). In the case of near stationary



238 convection and low-level flow, a forecaster might also use radial like propagation in this decision-  
239 making process, however, since convection geometry and low-level flow varies from storm to  
240 storm, only the first two steps are considered here. This approach aims to mirror the subjective  
241 process, leveraging the information content of optical flow to do so.

242 To handle the first step of line feature identification, a simple image line detection scheme was  
243 performed using the sum of a set of two-dimensional convolution kernels:

$$244 \quad a_1 = \begin{bmatrix} -1 & -1 & -1 \\ 2 & 2 & 2 \\ -1 & -1 & -1 \end{bmatrix} \quad a_2 = \begin{bmatrix} -1 & 2 & -1 \\ -1 & 2 & -1 \\ -1 & 2 & -1 \end{bmatrix} \quad a_3 = \begin{bmatrix} 2 & -1 & -1 \\ -1 & 2 & -1 \\ -1 & -1 & 2 \end{bmatrix} \quad a_4 = \begin{bmatrix} -1 & -1 & 2 \\ -1 & 2 & -1 \\ 2 & -1 & -1 \end{bmatrix}$$

245

246 Applying these kernels to the gaussian smoothed ABI visible imagery (using a 21x21 kernel and  
247 standard deviation of 5 pixels) results in high intensity values where line structures exist. A two-  
248 dimensional convolution threshold of 0.02 was used with the visible imagery calibrated to  
249 reflectance factor to isolate line features. This method was compared to a subjective interpretation  
250 of boundary location for validation.

251 To address the second step of the process, the constrained optical flow approach described in  
252 Section 3.1 was used to track the boundary pixels (both objectively and subjectively identified)  
253 back in time for three hours. The values of motion at each step in the backwards trajectory were  
254 determined with bilinear interpolation of the optical flow derived dense vector grid. If a back-  
255 traced pixel of the linear feature arrived within 50 km of a convective area with a  $10.35 \mu\text{m}$   
256 brightness temperature (BT<sub>10.35</sub>) lower than 223 K (-50 °C; using previous satellite imagery  
257 matched to the back-trajectory time), the original point was considered an OFB. While this  
258 brightness temperature threshold is subjective and can vary from case to case, it was found to  
259 produce a reasonable approximation of deep convection areas when compared to ground-based  
260 radar information for the case study described in the subsequent sections.



261    *3.3 Data*

262    The objective OFB identification methodology is tested using a case study from 5 July 2018  
263    over the southwestern United States. This event featured a distinct OFB and associated dust storm  
264    that was well-sampled by various ground- and space- based sensors. GOES-16 was in Mode-3,  
265    generating one image over the study area every 5-min (continental U.S., or CONUS, ABI scan  
266    domain). Optical flow computations employ the GOES-16 (GOES-East) ABI red band (0.64  $\mu$ m;  
267    ABI channel 2), provided at a nominal sub-satellite spatial resolution of 500 m, but closer to 1 km  
268    at the case study location. This channel is used at native resolution, though it can be subsampled  
269    with a low-pass filter such that future versions can implement color information from the blue and  
270    near-infrared bands (e.g. Miller et al. 2012). This means that the optical flow approach here is  
271    daytime only. A similar B04 approach can be used on infrared data as well for day/night  
272    independent information, though for detecting OFBs in the low levels, proxy visible products  
273    would perform best. As described above, the clean longwave infrared band (10.35  $\mu$ m; ABI  
274    channel 13) is used as first-order information on optically thick cloud-top heights and to assess the  
275    convective nature of the observed scene ( $BT_{10.35} < 223$  K).

276    High frequency Automated Surface Observing Stations (ASOS; NOAA 1998), recording  
277    temperature, pressure, wind speed and direction once every minute, complement the satellite  
278    imagery. The Weather Surveillance Radar-1988 Doppler (Crum and Alberty, 1993) dual-  
279    polarimetric data also sampled the OFB event from the KIWA radar near Phoenix, AZ. To  
280    highlight the OFBs and the presence of dust, horizontal reflectivity and correlation coefficient are  
281    used (Van Den Broeke and Alsarraf, 2016). Finally, for information on the full 3D dynamics of  
282    the case study, a numerical model representation of the environment was collected from the High  
283    Resolution Rapid Refresh system (HRRR, Benjamin et al. 2016). The combination of these model



284 and observation datasets is employed to confirm the presence of a distinct convective OFB, rather  
285 than some other quasi-linear feature, such as a bore or elevated cloud layer, etc.

286

#### 287 **4. Case Study Description**

288 Convection was observed in south central Arizona on 5 July 2018 after 1800 UTC. A large  
289 and well-defined linear structure emerged from below the convective cloud cover at 2200 UTC to  
290 6 July 2018 0100 UTC propagating westward in GOES-16 imagery (Fig. 3). This linear structure,  
291 demarcated by roll (arcus) clouds on the northern side and lofted dust on the southern side, was  
292 apparent with strong visible reflectance contrast against the relatively dark surface and  $BT_{10.35} \sim$   
293 10 K cooler than the underlying surface. The dust lofted by this outflow produced low visibility  
294 and hazardous driving conditions near Phoenix, AZ. Dust storm warnings were issued by the local  
295 National Weather Service (NWS) forecast office by 2300 UTC. The structure's observed radial  
296 propagation away from nearby deep convection and associated cloud and dust features lends to its  
297 interpretation as a convective OFB.

298 The OFB was also captured in radar scans from KIWA at 2200 UTC (Fig. 4). The coincidence  
299 of low correlation coefficient ( $< \sim 0.5$ ) and moderate to high reflectivity (near 20 dBZ) imply that  
300 the OFB was associated with airborne coarse dust particles. Surface observations taken at the  
301 ASOS station reveal temperatures exceeding 317 K (44 °C) ahead of the OFB, with calm winds  
302 (Fig. 5). Temperatures dropped by 4 K, wind speeds changed direction and increased sharply, and  
303 dew points increased rapidly as the OFB crossed the station at  $\sim 2316$  UTC. The rapid change in  
304 low-level meteorology is consistent with convective OFBs sampled in previous studies (e.g.  
305 Mahoney III, 1988; Miller et al., 2008).



306 The HRRR model captured the broad characteristics of this event (Fig. 6), showing moderate  
307 low-level winds in excess of  $10 \text{ m s}^{-1}$  (Fig. 6a), cooler temperatures (Fig. 6b), and simulated  
308 cumulus clouds from forced ascent (Fig. 6c). Model cross sections (Fig. 6d) indicated a moderate  
309 increase in vertical motion ahead of the numerically derived boundary, and a sharp decrease in  
310 virtual potential temperature behind the boundary. The shape of the virtual potential temperature  
311 profile is consistent with other model observations of OFBs (e.g. Chipilski et al., 2018). The  
312 observation and model data all show that the linear structure observed in Fig. 3 was modifying the  
313 dynamics of the surface in a manner consistent with OFBs, and not some other linear cloud feature  
314 type that is decoupled from the surface and may be misidentified by the satellite. Since such low-  
315 level linear features are often obscured by cloud layers at higher altitudes, this case study in some  
316 respects represents a best-case-scenario for evaluating optical flow capabilities towards identifying  
317 OFBs.

318

## 319 5. Results

320 The first step in OFB identification requires identification of a feature that appears linear in  
321 the imagery. Compared to the subjective boundary identification (considered as truth here; Fig 7a,  
322 blue dots), the convolution method gives a reasonable approximation to where the OFB is located  
323 within the higher intensity points in the convolution (Fig. 7b). Unfortunately, the simply-applied  
324 convolution is also sensitive to linear features associated with the deep convection itself (the blue  
325 shading in Fig. 7b). Hence, false alarms appear east of the boundary. These issues can be filtered  
326 out using either cloud-top height or brightness temperature thresholding from separate infrared  
327 channels. Alternatively, the storm-relative motion (here  $> 15 \text{ m s}^{-1}$ ) from optical flow was used  
328 here to filter the false alarms (the red shading in Fig. 7b).



329 The second step requires these linear fast-moving features to be traced backward to a deep  
330 convection source using the optical flow computation (Fig. 8). To the west of the boundary, near  
331 stationary optical flow vectors highlight the background (or ground) pixels. The boundary itself  
332 exhibits a westward movement near  $15-20 \text{ m s}^{-1}$  (~30-40 kts). The feature also appears to bow  
333 outwards after faster motions are observed, near  $33^\circ \text{ N}$ ,  $-112^\circ \text{ E}$  during 2338-2358 UTC (Figs. 8b,  
334 c). Similar westward motion is derived in the wake of the OFB, within the convective cold pool.  
335 This results from the presence of airborne dust particles, which facilitate the computation of optical  
336 flow vectors in this region.

337 The backwards trajectories of the subjectively and objectively identified OFB pixels in Figs.  
338 7c and d (B04 method) show that many of the linear cloud features, particularly those associated  
339 with the central arcus cloud, indeed originated near deep convection. However, when the  
340 backwards trajectories of the B04 method were compared to other optical flow methods, such as  
341 the approach by Wu et al. (2016), most were unsuccessful at obtaining coincidence between linear  
342 cloud features along the OFB and a deep convection source. Wu et al. (2016) used an approach  
343 introduced to the community by Farnebäck (2001), which is a *local* window method for optical  
344 flow.

345 Example points 1–7 examined within the subjectively identified OFB backward trajectories  
346 highlight an issue with *local* window approaches for this application (Fig. 9). The B04 approach  
347 (Fig. 9, blue/yellow) produced motions that were relatively consistent with the true boundary  
348 motion. Thus, many points that are lost in the *local* approaches are successfully backtracked to  
349 the initial deep convection (e.g. points 3–5). With the Wu et al. approach (Fig. 9, orange/red),  
350 OFB targets move slower than the actual boundary, and, over a three-hour tracking period,  
351 eventually become stuck within the stationary background pixels. This tracking issue stems from



352 an assumption made in many *local* approaches that pixels within an image window all move in the  
353 same direction with the same speed. When background pixels are included within an image  
354 window containing clouds or dust, the resulting optical flow speed would then be underestimated.  
355 The slow bias is observed in plots of optical flow speeds along the OFB (Fig. 10), where the Wu  
356 et al. approach was  $\sim$ 5-10 m s<sup>-1</sup> slower than the B04 approach. While not shown, we found similar  
357 backward trajectory issues using the LK approach. Full loops of the optical flow in Fig. 8 and  
358 trajectories in Fig. 9 are included as supplementary material to this manuscript.

359 For all approaches tested, however, methods struggled to backtrack the newly formed cumulus  
360 to the north and the dust front to the south. With the cumulus to the north, the issues with each  
361 algorithm appear to result from rapid cumulus development between frames (e.g. points 1 and 2 in  
362 Figs. 9a, b). Condensation like what is observed here is unfortunately not considered in the  
363 brightness constancy assumption. Thus, condensing cloud features would only be tracked back to  
364 when they initially form (after Fig. 9b) without additional dynamic constraints to Eq. (5). An  
365 example can be seen when points 1 and 2 become stuck in Fig. 9c. This has important implications  
366 on limitations of backtracking OFB features to deep convection with optical flow from imagery.  
367 If no cloud or dust feature exists to visualize an OFB in satellite imagery, some of the feature  
368 propagation may be lost.

369 The dust to the south appears in the satellite imagery as early as 2200 UTC, though it was quite  
370 transparent relative to the ground. It is therefore possible the stationary background pixels may be  
371 dominant in the optical flow computation at points 6 and 7, resulting in slower wind speeds than  
372 the true OFB propagation. Points 6 and 7 are also located near cumulus moving across the OFB  
373 motion to the south. This dust front tracking could be improved using multispectral techniques  
374 designed to highlight dust features over ground pixels, or by using additional color spectrum



375 information to discourage flow smoothness in Eq. (5) across the dust front from the cumulus to  
376 the south (e.g. Sun et al., 2010).

377 Many line-like targets east of the OFB in Fig. 7d also originated from the deep convection,  
378 which constitute false alarms. These false alarms can be reduced by further improving the OFB  
379 targeting step in the objective process in future studies. For this case study, it may have been  
380 possible to use convergence methods, analogous to radar-based objective OFB identification, to  
381 isolate the boundary. However, convergence as derived from the optical flow information here  
382 would only work because of local, stationary background pixels ahead of the OFB. This means  
383 that convergence would almost always be inferred from OFB motion when the background is  
384 involved. This approach would also be sensitive to nearby cloud structures ahead of the OFB  
385 which would exhibit different (non-stationary) motion from the background. It is for this reason  
386 that a backwards trajectory approach was elected instead of basing the detection on local horizontal  
387 convergence. The optical flow approach used here does help highlight the OFB when storm  
388 motion alone was considered in addition to convolution, showing how additional tools can be used  
389 in synergy to arrive at a more comprehensive objective feature identification approach in future  
390 studies.

391

## 392 **6. Conclusions and Future Outlook**

393 A new method for the objective identification of outflow boundaries (OFBs) in GOES-16  
394 Advanced Baseline Imager (ABI) data was developed using optical flow motion derivation  
395 algorithms and demonstrated with provisional success on a dust storm case study. An optical flow  
396 system constructed for this purpose shows promise in identifying and backtracking object events  
397 to their source over traditional flow derivation methods, which can potentially be used to isolate



398 convective OFB features. To the best of the authors' knowledge, this study represents a first  
399 attempt to objectively identify OFBs in geostationary satellite imagery.

400 The primary conclusions of this study are that optical flow approaches are now a viable option  
401 to acquire meso-scale flows relevant to OFB tracking and detection in 5-min geostationary satellite  
402 imagery, though the successful backtracking of OFB features requires use of flow algorithms that  
403 can handle the presence of motion discontinuities and stationary background flow. The optical  
404 flow algorithm tested in this study produced a dense motion field that was closer than other  
405 methods to the true OFB motion and provided valuable information towards full objective OFB  
406 identification in new products.

407 While several OFB related image pixels were successfully identified, the algorithm here is  
408 relatively immature and remains fraught with false alarms where linear features are incorrectly  
409 identified, and where correct features were not successfully backtracked to deep convection. The  
410 algorithm is still limited by the assumptions made within optical flow, which only account for  
411 changes in image brightness intensity resulting from pure feature advection. Therefore, if no  
412 features (e.g. clouds) exist to highlight an OFB boundary within the imagery, the method proposed  
413 here would not function properly. The method also struggles to resolve true OFB motions with  
414 transparent dust movement, where a textured background beneath the dust may dominate the  
415 motion estimate within a scene. Also, while infrared brightness temperature was enough to  
416 identify deep convection in this case study, convection may be missed by brightness temperature  
417 imagery if it is obscured by a higher cloud layer, or if the minimum cloud-top brightness  
418 temperature exceeds an arbitrarily set threshold.

419 Given these limitations, future studies will explore more advanced systems for linear structure  
420 identification to identify candidate features for tracking towards full objective OFB identification.



421 A machine learning system will be used to determine which linear characteristics of the image  
422 should be backtracked instead of using two-dimensional convolution. Optical flow can be used to  
423 precondition training information for a machine learning approach, if motion or semi-Lagrangian  
424 fields are needed. Furthermore, it will be prudent to use deep convection correspondence through  
425 optical flow backtracking as one of many fields in future products, such as radial propagation away  
426 from storms and near surface meteorological properties, to probabilistically decide if an image  
427 pixel is associated with an OFB. To better identify deep convection areas, the GOES Lightning  
428 Mapper (GLM) can be used, which provides information on lightning location and energy at 8 km  
429 resolution with a 2 ms frame rate.

430 Feature identification with optical flow is not restricted to OFBs alone. For example, the  
431 above-anvil cirrus plume (Bedka et al., 2018) over deep convection has been identified as an  
432 important indicator of severe weather at the ground, yet no objective means of identification exists  
433 today. The properties from optical flow could be used as an additional source of information in  
434 such algorithm designs, allowing researchers to backtrack features to their apparent source (the  
435 overshooting top in the case of the above-anvil cirrus plume) and monitor cloud temperature and  
436 visible texture trends, or to simply use the dense motion itself to achieve better results. This  
437 method will also be applicable to other cold pool outflow phenomena, such as bores, for which  
438 new algorithms could utilize numerical model or surface observations for further clarification of  
439 linear feature type.

440 Motion discontinuity preserving optical flow will also benefit several current algorithms for  
441 monitoring deep convection in satellite imagery. Objective deep convection cloud-top flow field  
442 algorithms (Apke et al., 2016, 2018) will benefit particularly when sharp cloud-edges and ground  
443 pixels are present in an image scene. Systems that use infrared cloud-top cooling or emissivity



444 differences for deep convection nowcasting will also improve with better estimates of pre-  
445 convective cumulus motion (Cintineo et al., 2014; Mecikalski and Bedka, 2006).

446 While the utility of a backwards trajectory approach was considered here, many other possible  
447 methods exist for exploiting the semi-Lagrangian properties of time-resolved observations in  
448 satellite imagery (e.g. Nisi et al., 2014). Use of fine-temporal resolution information will improve  
449 optical flow estimates, and in turn the estimates of brightness temperature, reflectance, or cloud-  
450 property changes in a moving frame of reference. We will explore these and other refinements in  
451 ongoing and future work on this exciting frontier of next-generation ABI-enabled science.

452

## 453 7. Data Availability

454 Data used in this study are available upon request by contacting the lead author.

455

## 456 8. Author Contributions

457 JMA developed the primary code for the optical flow approach used here. He also co-  
458 developed the objective outflow boundary identification techniques, and related Figs. (1, 2, 3, 7-  
459 10) in the manuscript. He co-wrote much of the text and led the efforts of interpretation, analysis,  
460 and presentation of the results.

461 KAH was responsible for case study identification, and collection of surface, radar, and HRRR  
462 data relevant to this case study. He developed Figs. 4, 5 and 6. He also co-developed the objective  
463 OFB identification process and co-wrote the text.

464 SDM was the PI of the Multidisciplinary University Research Initiative (MURI) research  
465 project and was responsible for managing the development of the optical flow code and outflow  
466 boundary case study information involved in Figs. (1, 2, 3, 7-10). He co-developed the objective



467 identification process and maintained and managed the satellite data necessary to complete the  
468 study. He also co-wrote much of the text within the manuscript.

469 DAP co-developed the objective OFB identification scheme. He also co-developed the  
470 conceptual Figs. 1 and 2 to add clarity to the optical flow process used here and co-wrote the text  
471 within the manuscript.

472

#### 473 **9. Competing Interests**

474 The authors declare that they have no conflicts of interest.

475

#### 476 **10. Acknowledgements**

477 This CIRA team was funded by the Multidisciplinary University Research Initiative (MURI) grant  
478 N00014-16-1-2040. David Peterson was supported by the National Aeronautics and Space  
479 Administration (NASA) award NNH17ZDA001N. Our special thanks to Dan Bikos and Curtis  
480 Seaman at the Cooperative Institute for Research in the Atmosphere for informative discussions  
481 on identification of outflow boundaries in satellite imagery. We also thank Max Marchand for  
482 providing the high-frequency surface observations used in this study.



483 11. References

484 Anandan, P.: A computational framework and an algorithm for the measurement of visual  
485 motion, *Int. J. Comput. Vis.*, 2(3), 283–310, doi:10.1007/BF00158167, 1989.

486 Apke, J. M., Mecikalski, J. R. and Jewett, C. P.: Analysis of Mesoscale Atmospheric Flows  
487 above Mature Deep Convection Using Super Rapid Scan Geostationary Satellite Data, *J. Appl.*  
488 *Meteorol. Climatol.*, 55(9), 1859–1887, doi:10.1175/JAMC-D-15-0253.1, 2016.

489 Apke, J. M., Mecikalski, J. R., Bedka, K. M., McCaul Jr., E. W., Homeyer, C. R. and Jewett, C.  
490 P.: Relationships Between Deep Convection Updraft Characteristics and Satellite Based Super  
491 Rapid Scan Mesoscale Atmospheric Motion Vector Derived Flow, *Mon. Wea. Rev.*, Submitted,  
492 doi:10.1175/MWR-D-18-0119.1, 2018.

493 Associated Press: Sheriff: 11 people dead after Missouri tourist boat accident, *Assoc. Press*  
494 [online] Available from: <https://www.apnews.com/a4031f35b4744775a7f59216a56077ed>, 2018.

495 Barron, J. L., Fleet, D. J. and Beauchemin, S. S.: Performance of Optical Flow Techniques, *Int.*  
496 *J. Comput. Vis.*, 12, 43–77, 1994.

497 Bedka, K. M., Velden, C. S., Petersen, R. A., Feltz, W. F. and Mecikalski, J. R.: Comparisons of  
498 satellite-derived atmospheric motion vectors, rawinsondes, and NOAA wind profiler  
499 observations, *J. Appl. Meteorol. Climatol.*, 48(8), 1542–1561, doi:10.1175/2009JAMC1867.1,  
500 2009.

501 Bedka, K. M., Murillo, E., Homeyer, C. R., Scarino, B. and Mersiovski, H.: The Above Anvil  
502 Cirrus Plume: The Most Definitive Severe Weather Indicator from Visible and Infrared Satellite  
503 Imagery, *J. Appl. Meteor.*, In Prep, 2018.

504 Benjamin, S. G., Weygandt, S. S., Brown, J. M., Hu, M., Alexander, C., Smirnova, T. G., Olson,  
505 J. B., James, E., Dowell, D. C., Grell, G. A., Lin, H., Peckham, S. E., Smith, T. L., Moninger, W.  
506 R., Kenyon, J. and Manikin, G. S.: A North American Hourly Assimilation and Model Forecast  
507 Cycle: The Rapid Refresh, *Mon. Weather Rev.*, 144(4), 1669–1694, doi:10.1175/MWR-D-15-  
508 0242.1, 2016.

509 Black, M. J. and Anandan, P.: The robust estimation of multiple motions: Parametric and  
510 piecewise-smooth flow fields, *Comput. Vis. Image Underst.*, doi:10.1006/cviu.1996.0006, 1996.

511 Bresky, W. C. and Daniels, J.: The feasibility of an optical flow algorithm for estimating  
512 atmospheric motion, *Proc. Eighth Int. Wind. Work.*, 24–28, 2006.

513 Bresky, W. C., Daniels, J. M., Bailey, A. A. and Wanzong, S. T.: New methods toward  
514 minimizing the slow speed bias associated with atmospheric motion vectors, *J. Appl. Meteorol.*  
515 *Climatol.*, 51(12), 2137–2151, doi:10.1175/JAMC-D-11-0234.1, 2012.

516 Van Den Broeke, M. S. and Alsarraf, H.: Polarimetric Radar Observations of Dust Storms at C-  
517 and S-Band, *J. Oper. Meteor.*, 4(9), 123–131, 2016.

518 Brox, T.: From Pixels to Regions: Partial Differential Equations in Image Analysis, Ph.D. thesis,  
519 Saarland University, Saarbrücken, Germany., 2005.

520 Brox, T., Bruhn, A., Papenberg, N. and Weickert, J.: High accuracy optical flow estimation



521 based on a theory for warping, 2004 *Eur. Conf. Comput. Vis.*, 4(May), 25–36, 2004.

522 Byers, H. R. and Braham Jr., R. R.: *The Thunderstorm*, U.S. Thund., U.S. Gov't. Printing Office,  
523 Washington D.C., 1949.

524 Chipilski, H. G., Wang, X. and Parsons., D. P.: An Object-Based Algorithm for the Identification  
525 and Tracking of Convective Outflow Boundaries, *Mon. Weather Rev.*, 1–57, doi:10.1175/MWR-D-18-0116.1, 2018.

527 Cintineo, J. L., Pavolonis, M. J., Sieglaff, J. M. and Lindsey, D. T.: An Empirical Model for  
528 Assessing the Severe Weather Potential of Developing Convection, *Weather Forecast.*, 29(3),  
529 639–653, doi:10.1175/WAF-D-13-00113.1, 2014.

530 Crum, T. D. and Alberty, R. L.: The WSR-88D and the WSR-88D Operational Support Facility,  
531 *Bull. Am. Meteorol. Soc.*, 74(9), 1669–1687, doi:10.1175/1520-0477, 1993.

532 Farnebäck, G.: Two-Frame Motion Estimation Based on Polynomial Expansion, in *Proceedings: Eighth IEEE International Conference on Computer Vision*, vol. 1, pp. 171–177., 2001.

534 Fleet, D. and Weiss, Y.: Optical Flow Estimation, *Math. Model. Comput. Vis. Handb.*, 239–257,  
535 doi:10.1109/TIP.2009.2032341, 2005.

536 Hardy, K. and Comfort, L. K.: Dynamic decision processes in complex, high-risk operations:  
537 The Yarnell Hill Fire, June 30, 2013, *Saf. Sci.*, 71(Part A), 39–47,  
538 doi:10.1016/j.ssci.2014.04.019, 2015.

539 Héas, P., Mémin, E., Papadakis, N. and Szantai, A.: Layered estimation of atmospheric  
540 mesoscale dynamics from satellite imagery, *IEEE Trans. Geosci. Remote Sens.*, 45(12), 4087–  
541 4104, doi:10.1109/TGRS.2007.906156, 2007.

542 Hermes, L. G., Witt, A., Smith, S. D., Klingele-Wilson, D., Morris, D., Stumpf, G. and Elts, M.  
543 D.: The Gust-Front Detection and Wind-Shift Algorithms for the Terminal Doppler Weather  
544 Radar System, *J. Atmos. Ocean. Technol.*, 10, 693–709, 1993.

545 Horn, B. K. P. and Schunck, B. G.: Determining optical flow, *Artif. Intell.*, 17(1–3), 185–203,  
546 doi:10.1016/0004-3702(81)90024-2, 1981.

547 Idso, S. B., Ingram, R. S. and Pritchard, J. M.: An American Haboob, *Bull. Am. Meteorol. Soc.*,  
548 53(10), 930–935, doi:10.1175/1520-0477(1972)053<0930:AAH>2.0.CO;2, 1972.

549 Johnson, R. H., Schumacher, R. S., Ruppert, J. H., Lindsey, D. T., Ruthford, J. E. and  
550 Kriederman, L.: The Role of Convective Outflow in the Waldo Canyon Fire, *Mon. Weather  
551 Rev.*, 142(9), 3061–3080, doi:10.1175/MWR-D-13-00361.1, 2014.

552 Klingele, D. L., Smith, D. R. and Wolfson, M. M.: Gust Front Characteristics as Detected by  
553 Doppler Radar, *Mon. Weather Rev.*, 115(5), 905–918, doi:10.1175/1520-  
554 0493(1987)115<0905:gfcadb>2.0.co;2, 1987.

555 Line, W. E., Schmit, T. J., Lindsey, D. T. and Goodman, S. J.: Use of Geostationary Super Rapid  
556 Scan Satellite Imagery by the Storm Prediction Center\*, *Weather Forecast.*, 31(2), 483–494,  
557 doi:10.1175/WAF-D-15-0135.1, 2016.

558 Mahoney III, W.: Gust front characteristics and the kinematics associated with interacting



559 thunderstorm outflows, *Mon. Weather Rev.*, 116(7), 1474–1492 [online] Available from:  
560 [http://journals.ametsoc.org/doi/abs/10.1175/1520-0493\(1988\)116%3C1474%3AGFCATK%3E2.0.CO%3B2](http://journals.ametsoc.org/doi/abs/10.1175/1520-0493(1988)116%3C1474%3AGFCATK%3E2.0.CO%3B2), 1988.

562 Mecikalski, J. R. and Bedka, K. M.: Forecasting Convective Initiation by Monitoring the  
563 Evolution of Moving Cumulus in Daytime GOES Imagery, *Mon. Weather Rev.*, 134, 49–78,  
564 doi:10.1175/MWR3062.1, 2006.

565 Mecikalski, J. R., Jewett, C. P., Apke, J. M. and Carey, L. D.: Analysis of Cumulus Cloud  
566 Updrafts as Observed with 1-Min Resolution Super Rapid Scan GOES Imagery, *Mon. Wea.  
567 Rev.*, 144(2015), 811–830, doi:10.1175/MWR-D-14-00399.1, 2016.

568 Miller, S. D., Kuciauskas, A. P., Liu, M., Ji, Q., Reid, J. S., Breed, D. W., Walker, A. L. and  
569 Mandoos, A. Al: Haboob dust storms of the southern Arabian Peninsula, *J. Geophys. Res.  
570 Atmos.*, 113(1), 1–26, doi:10.1029/2007JD008550, 2008.

571 Miller, S. D., Schmidt, C. C., Schmit, T. J. and Hillger, D. W.: A case for natural colour imagery  
572 from geostationary satellites, and an approximation for the GOES-R ABI, *Int. J. Remote Sens.*,  
573 33(13), 3999–4028, doi:10.1080/01431161.2011.637529, 2012.

574 Mitchell, K. E. and Hovermale, J. B.: A Numerical Investigation of the Severe Thunderstorm  
575 Gust Front, *Mon. Weather Rev.*, 105(5), 657–675, doi:10.1175/1520-0493(1977)105<0657:aniots>2.0.co;2, 1977.

577 Mueller, C., Saxen, T., Roberts, R., Wilson, J., Betancourt, T., Dettling, S., Oien, N. and Yee, J.:  
578 NCAR Auto-Nowcast System, *Weather Forecast.*, 18(4), 545–561, doi:10.1175/1520-0434(2003)018<0545:NAS>2.0.CO;2, 2003.

580 Nieman, S. J., Menzel, W. P., Hayden, C. M., Gray, D., Wanzong, S. T., Velden, C. S. and  
581 Daniels, J.: Fully automatic cloud drift winds in NESDIS operations, *Bull. Am. Meteorol. Soc.*,  
582 78(6), 1121–1133, 1997.

583 Nisi, L., Ambrosetti, P. and Clementi, L.: Nowcasting severe convection in the Alpine region:  
584 The COALITION approach, *Q. J. R. Meteorol. Soc.*, 140(682), 1684–1699, doi:10.1002/qj.2249,  
585 2014.

586 NOAA: Automated Surface Observing System user's guide. National Oceanic and Atmospheric  
587 Administration, 61 pp + appendixes. [Available online at  
588 <http://www.nws.noaa.gov/asos/pdfs/aum-toc.pdf>.], 1998.

589 Peterson, D. A., Hyer, E. J., Campbell, J. R., Fromm, M. D., Hair, J. W., Butler, C. F. and Fenn,  
590 M. A.: The 2013 Rim Fire: Implications for predicting extreme fire spread, pyroconvection,  
591 smoke emissions, *Bull. Am. Meteorol. Soc.*, 96(2), 229–247, doi:10.1175/BAMS-D-14-00060.1,  
592 2015.

593 Peterson, D. A., Fromm, M. D., Solbrig, J. E., Hyer, E. J., Surratt, M. L. and Campbell, J. R.:  
594 Detection and inventory of intense pyroconvection in western North America using GOES-15  
595 daytime infrared data, *J. Appl. Meteorol. Climatol.*, 56(2), 471–493, doi:10.1175/JAMC-D-16-  
596 0226.1, 2017.

597 Peterson, D. A., Campbell, J. R., Hyer, E. J., Fromm, M. D., Kablick, G. P., Cossuth, J. H. and  
598 DeLand, M. T.: Wildfire-driven thunderstorms cause a volcano-like stratospheric injection of



599 smoke, NPJ Clim. Atmos. Sci., 1(1), 1–8, doi:10.1038/s41612-018-0039-3, 2018.

600 Press, W. H., Flannery, B. P., Teukolsky, S. A. and Vetterling, W. T.: Numerical recipes in C:  
601 the art of scientific programming., 1992.

602 Raman, A., Arellano, A. F. and Brost, J. J.: Revisiting haboobs in the southwestern United  
603 States: An observational case study of the 5 July 2011 Phoenix dust storm, Atmos. Environ., 89,  
604 179–188, doi:10.1016/j.atmosenv.2014.02.026, 2014.

605 Roberts, R. D., Anderson, A. R. S., Nelson, E., Brown, B. G., Wilson, J. W., Pocernich, M. and  
606 Saxen, T.: Impacts of Forecaster Involvement on Convective Storm Initiation and Evolution  
607 Nowcasting, Weather Forecast., 27(5), 1061–1089, doi:10.1175/WAF-D-11-00087.1, 2012.

608 Schmit, T. J., Goodman, S. J., Lindsey, D. T., Rabin, R. M., Bedka, K. M., Gunshor, M. M.,  
609 Cintineo, J. L., Velden, C. S., Scott Bachmeier, A., Lindstrom, S. S. and Schmidt, C. C.:  
610 Geostationary Operational Environmental Satellite (GOES)-14 super rapid scan operations to  
611 prepare for GOES-R, J. Appl. Remote Sens., 7(1), 073462–073462,  
612 doi:10.1111/1.JRS.7.073462, 2013.

613 Schmit, T. J., Griffith, P., Gunshor, M. M., Daniels, J. M., Goodman, S. J. and Lebair, W. J.: A  
614 Closer Look at the ABI on the GOES-R Series, Bull. Am. Meteorol. Soc., doi:10.1175/BAMS-  
615 D-15-00230.1, 2016.

616 Sieglaff, J. M., Hartung, D. C., Feltz, W. F., Cronce, L. M. and Lakshmanan, V.: A satellite-  
617 based convective cloud object tracking and multipurpose data fusion tool with application to  
618 developing convection, J. Atmos. Ocean. Technol., 30(3), 510–525, doi:10.1175/JTECH-D-12-  
619 00114.1, 2013.

620 Sun, D., Roth, S. and Black, M. J.: Secrets of optical flow estimation and their principles, in  
621 Proceedings of the IEEE Computer Society Conference on Computer Vision and Pattern  
622 Recognition., 2010.

623 Uyeda, H. and Zrnić, D. S.: Automatic Detection of Gust Fronts, J. Atmos. Ocean. Technol., 3,  
624 36–50, 1986.

625 Velden, C. S., Hayden, C. M., Nieman, S. J., Menzel, W. P., Wanzong, S. and Goerss, J. S.:  
626 Upper-Tropospheric Winds Derived from Geostationary Satellite Water Vapor Observations,  
627 Bull. Am. Meteorol. Soc., 78(2), 173–195, 1997.

628 Velden, C. S., Daniels, J., Stettner, D., Santek, D., Key, J., Dunion, J., Holmlund, K., Dengel, G.,  
629 Bresky, W. and Menzel, P.: Recent-innovations in deriving tropospheric winds from  
630 meteorological satellites, Bull. Am. Meteorol. Soc., 86(2), 205–223, doi:10.1175/BAMS-86-2-  
631 205, 2005.

632 Wu, Q., Wang, H.-Q., Lin, Y.-J., Zhuang, Y.-Z. and Zhang, Y.: Deriving AMVs from  
633 Geostationary Satellite Images Using Optical Flow Algorithm Based on Polynomial Expansion,  
634 J. Atmos. Ocean. Technol., 33(8), 1727–1747, doi:10.1175/JTECH-D-16-0013.1, 2016.

635 Yin, D., Nickovic, S., Barbaris, B., Chandy, B. and Sprigg, W. A.: Modeling wind-blown desert  
636 dust in the southwestern United States for public health warning: A case study, Atmos. Environ.,  
637 39(33), 6243–6254, doi:10.1016/j.atmosenv.2005.07.009, 2005.



638 **12. List of Tables**

639 **Table 1.** Settings used in the Brox et al. (2004) successive over-relaxation scheme.

640



641 **13. List of Figures**

642 **Figure 1.** Flow chart of the B04 optical flow approach used here. Note that SF, nK, nL and nM  
643 are defined in Table 1.

644 **Figure 2.** Schematic of coarse- to fine-scale warping optical flow in GOES-imagery. The largest  
645 displacements are found in the initial coarse grid (yellow arrow at the top of the pyramid), which  
646 are used as initial displacements for the next levels (red and blue arrows). The final  
647 displacement is the sum of each displacement estimate (white arrow). In this schematic, an  
648 example scale factor of 0.5 was used over 3 pyramid levels, in this work, a scale factor of 0.95  
649 for 77 levels was used.

650 **Figure 3.** The 6 July 2018 0023 UTC GOES-16 0.64- $\mu$ m visible reflectance (top) and BT<sub>10.35</sub>  
651 (bottom) over south-central AZ, centered on an OFB of interest.

652 **Figure 4.** The KIWA Radar 2244 UTC 0.5° horizontal reflectivity (top) in dBZ and correlation  
653 coefficient (bottom). Range rings in grey indicate every 30° azimuth and 50 km in range.

654 **Figure 5.** Surface High Frequency METAR observations of temperature (K; top left), dewpoint  
655 (K; top right), mean sea level pressure (middle left), wind direction (° from N; middle right),  
656 wind speed (m s<sup>-1</sup>; bottom left), and wind gusts (m s<sup>-1</sup>; bottom right). The surface station was  
657 located at (32.95 °N -111.77 °E). The red line indicates the approximate time of boundary  
658 passage over the station.

659 **Figure 6.** Four panel of HRRR output of OFB event, including a) wind speed, b) temperature, c)  
660 simulated infrared brightness temperature, and d) a cross section along the black line in c with  
661 virtual potential temperature  $\theta_v$  in black contours (K), omega in color shaded pixels, and regions  
662 of relative humidity > 90% highlighted with dark shading (bottom right).



663 **Figure 7.** The 0023 UTC GOES-16 0.64- $\mu$ m visible channel shown with a) subjectively  
664 identified OFB (blue dots) and b) objectively identified linear features (blue shading). Also  
665 shown are linear features that contained fast storm-relative motion (red shading). The results of  
666 backtracking the c) subjectively and d) objectively identified OFB features are also shown,  
667 where blue dots represent targets tracked back within 50 km of a deep convection event, and  
668 orange dots are targets that were not.

669 **Figure 8.** GOES-16 0.64- $\mu$ m visible channel imagery on 5 July 2018 at a) 2258 UTC, b) 2338  
670 UTC, c) 2358 UTC, and d) 0023 UTC over central Arizona shown with every 20<sup>th</sup> optical flow  
671 vector in the x and y directions (subsampled for image clarity) illustrated with yellow wind bars  
672 (knots). Circles represent motion < 5 kts, which commonly occur over ground pixels.

673 **Figure 9.** The GOES-16 0.64- $\mu$ m visible imagery shown with image targets backtracked from  
674 subjective identification in Fig. 7a at 0023 UTC 6 July 2018 using the B04 method (blue/yellow)  
675 and the Wu et al. (2016) approach (orange/red) at a) 0023 UTC, b) 2358 UTC, c) 2338 UTC and  
676 d) 2213 UTC. Individual points are highlighted from each approach (yellow and red dots; see  
677 text).

678 **Figure 10.** Color shaded wind speed for 0023 UTC 6 July 2018 over central Arizona shown  
679 from a) the B04 optical flow method and b) the Wu et al. (2016) flow, shown with respective  
680 flow vectors and the subjective position of the front edge of the OFB (blue line).

681  
682



683 **14. Tables**

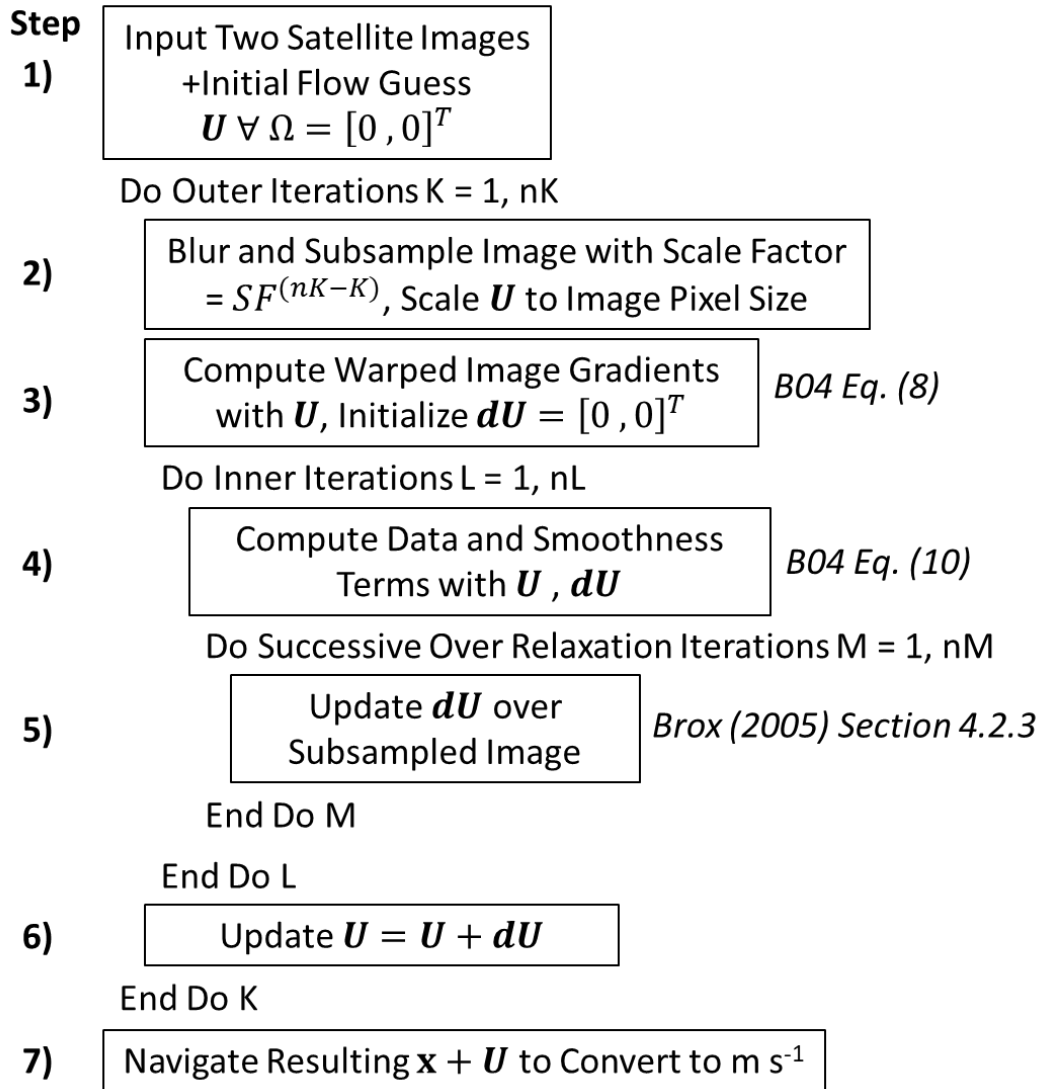
684 **Table 1.** Settings used in the Brox et al. (2004) successive over-relaxation scheme.

Parameter	Value
Outer Iterations (Pyramid Levels, nK)	77
Inner Iterations (nL)	10
Successive Over-Relaxation Iterations (nM)	5
Successive Over-Relaxation Parameter	1.99
Pyramid Scale Factor (SF)	0.95
$\gamma$	10
$\alpha$	50

685

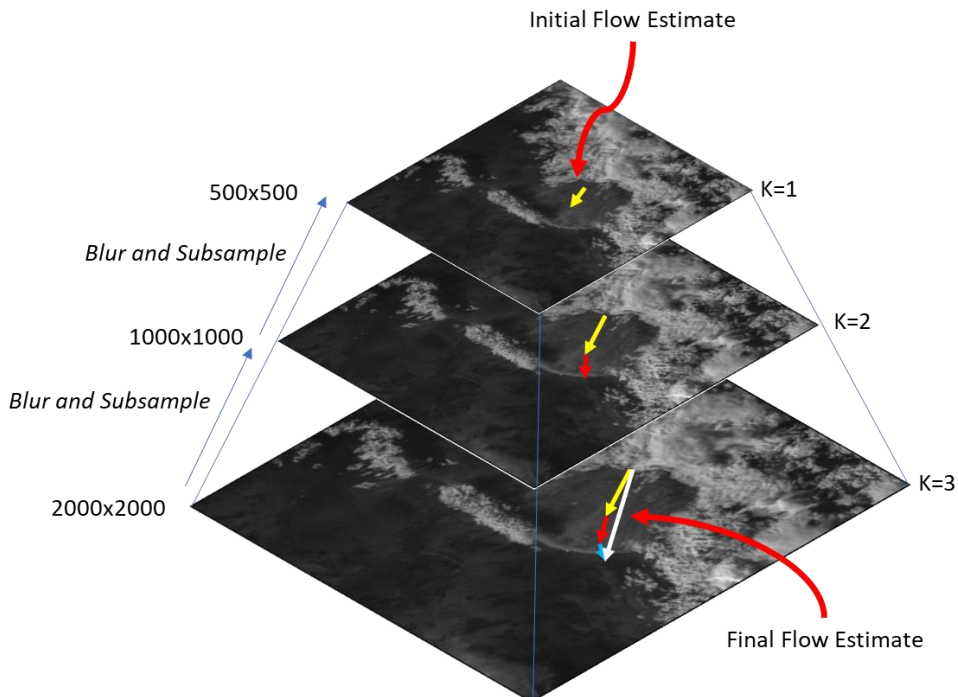


686 15. Figures



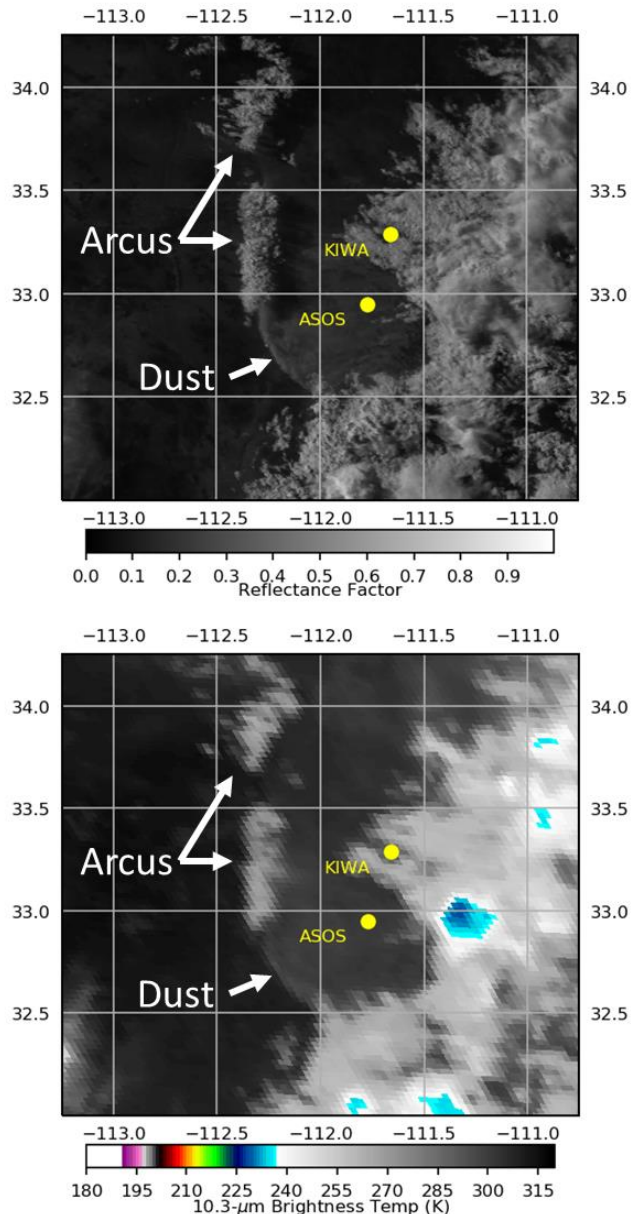
687

688 **Figure 1.** Flow chart of the B04 optical flow approach used here. Note that SF, nK, nL and nM  
689 are defined in Table 1.  
690



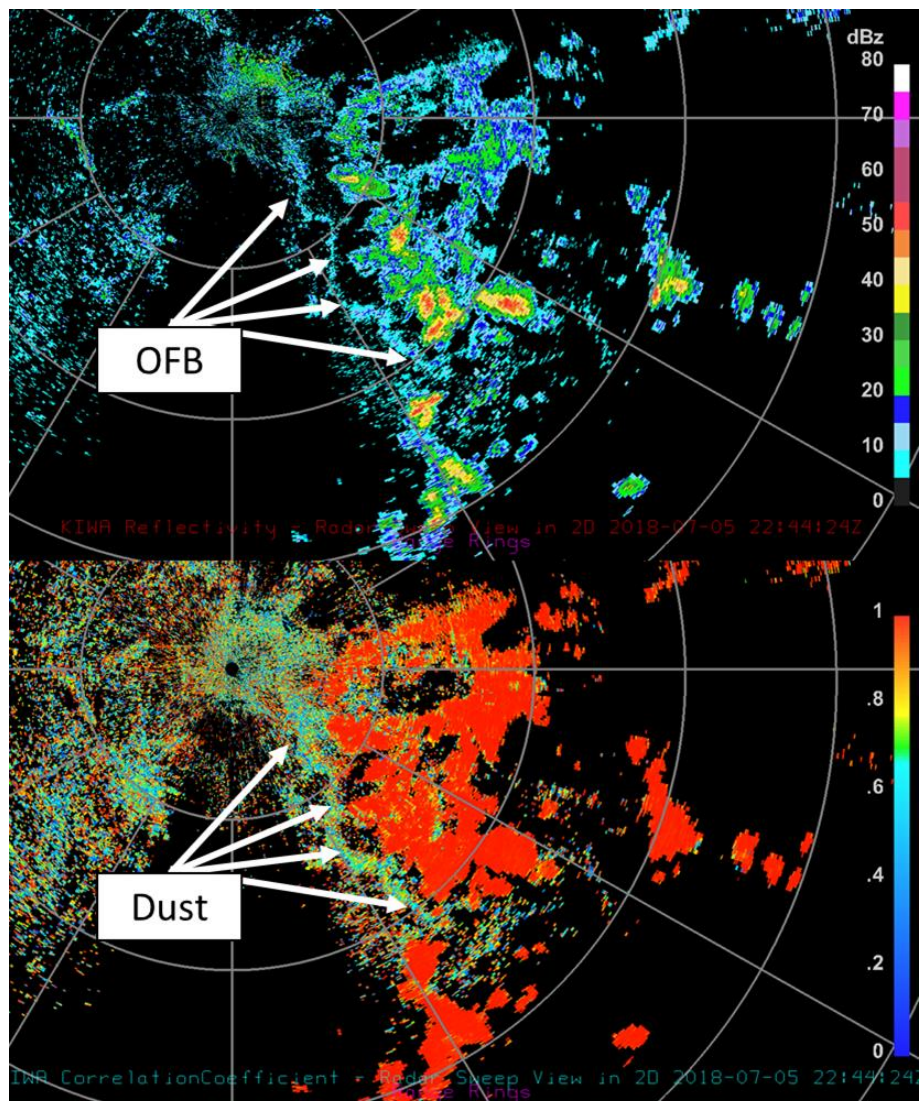
691

692 **Figure 2.** Schematic of coarse- to fine-scale warping optical flow in GOES-imagery. The largest  
693 displacements are found in the initial coarse grid (yellow arrow at the top of the pyramid), which  
694 are used as initial displacements for the next levels (red and blue arrows). The final  
695 displacement is the sum of each displacement estimate (white arrow). In this schematic, an  
696 example scale factor of 0.5 was used over 3 pyramid levels, in this work, a scale factor of 0.95  
697 for 77 levels was used.  
698



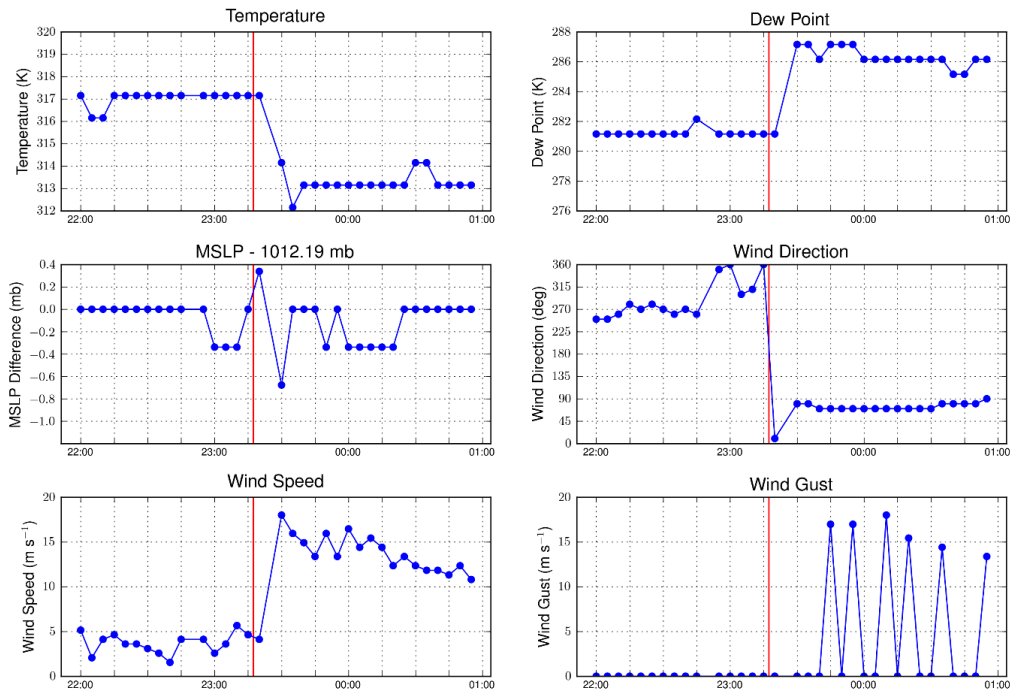
699

700 **Figure 3.** The 6 July 2018 0023 UTC GOES-16 0.64- $\mu$ m visible reflectance (top) and BT<sub>10.35</sub>  
701 (bottom) over south-central AZ, centered on an OFB of interest.  
702



703

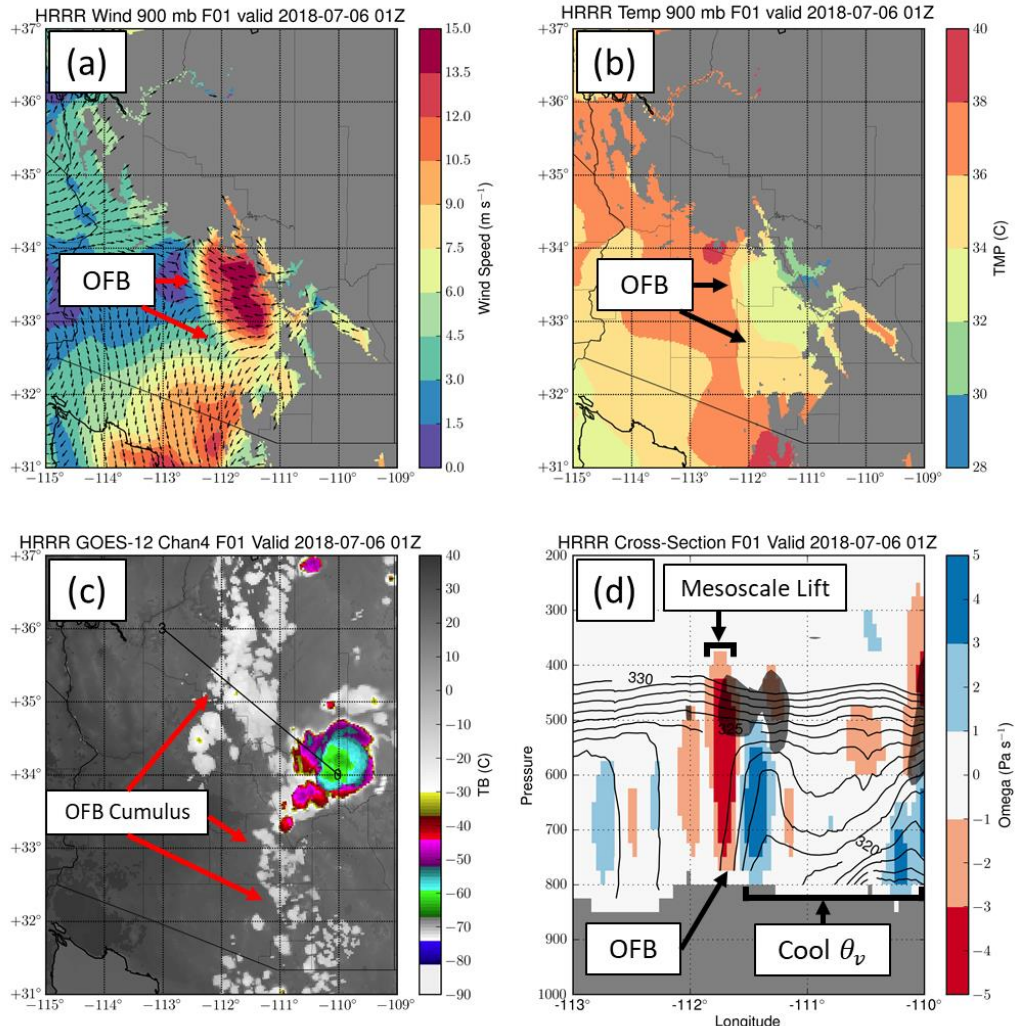
704 **Figure 4.** The KIWA Radar 2244 UTC 0.5° horizontal reflectivity (top) in dBZ and correlation  
705 coefficient (bottom). Range rings in grey indicate every 30° azimuth and 50 km in range.  
706



707

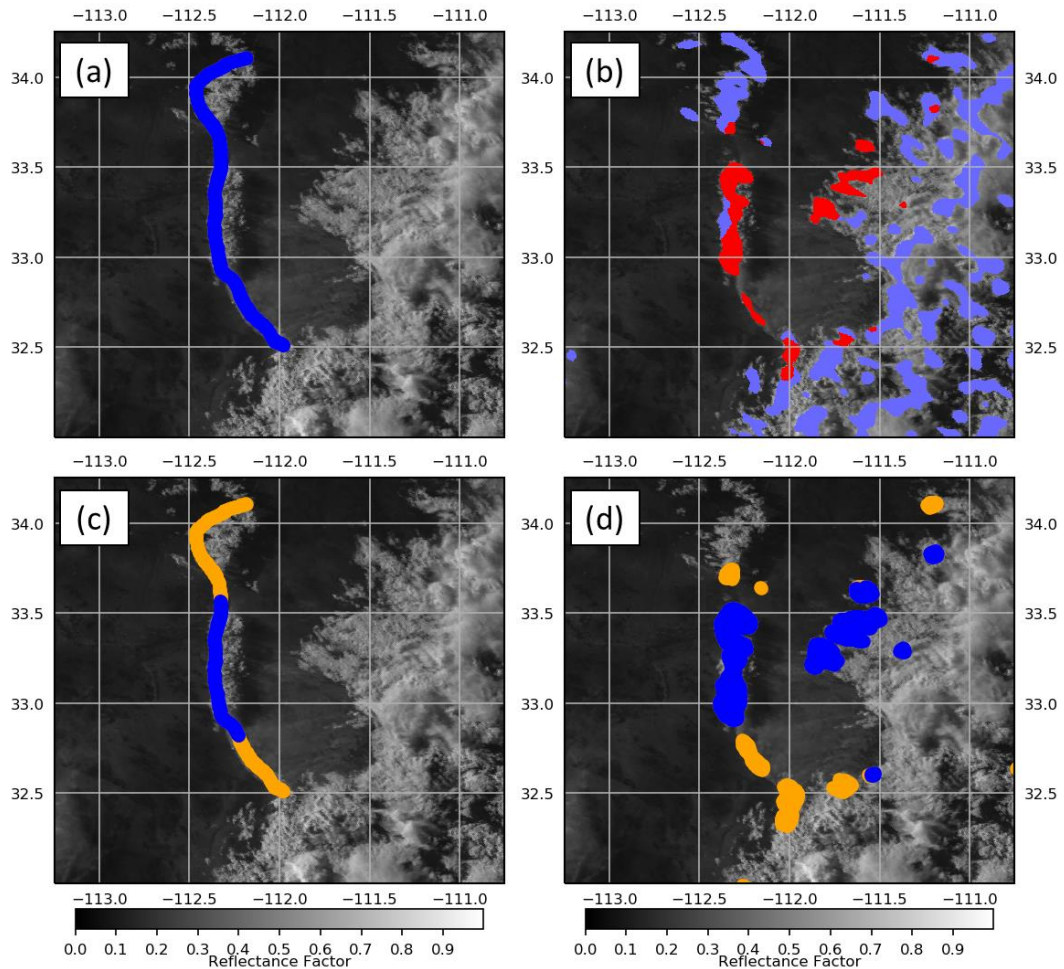
708 **Figure 5.** Surface High Frequency METAR observations of temperature (K; top left), dewpoint  
709 (K; top right), mean sea level pressure (middle left), wind direction ( $^{\circ}$  from N; middle right),  
710 wind speed ( $m s^{-1}$ ; bottom left), and wind gusts ( $m s^{-1}$ ; bottom right). The surface station was  
711 located at (32.95  $^{\circ}$ N -111.77  $^{\circ}$ E). The red line indicates the approximate time of boundary  
712 passage over the station.

713



714

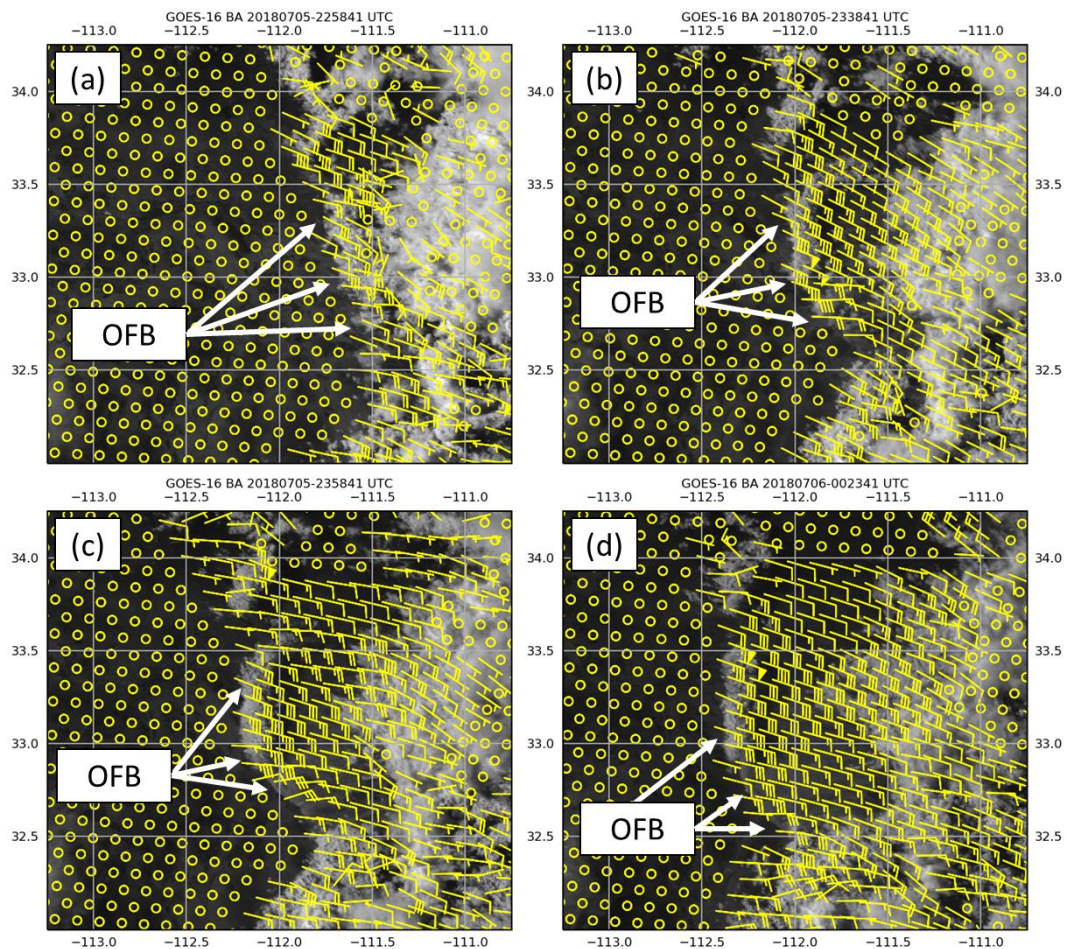
715 **Figure 6.** Four panel of HRRR output of OFB event, including a) wind speed, b) temperature,  
 716 c) simulated infrared brightness temperature, and d) a cross section along the black line in c with  
 717 virtual potential temperature  $\theta_v$  in black contours (K), omega in color shaded pixels, and regions  
 718 of relative humidity > 90% highlighted with dark shading (bottom right).  
 719



720

721 **Figure 7.** The 0023 UTC GOES-16 0.64-μm visible channel shown with a) subjectively  
722 identified OFB (blue dots) and b) objectively identified linear features (blue shading). Also  
723 shown are linear features that contained fast storm-relative motion (red shading). The results of  
724 backtracking the c) subjectively and d) objectively identified OFB features are also shown,  
725 where blue dots represent targets tracked back within 50 km of a deep convection event, and  
726 orange dots are targets that were not.

727

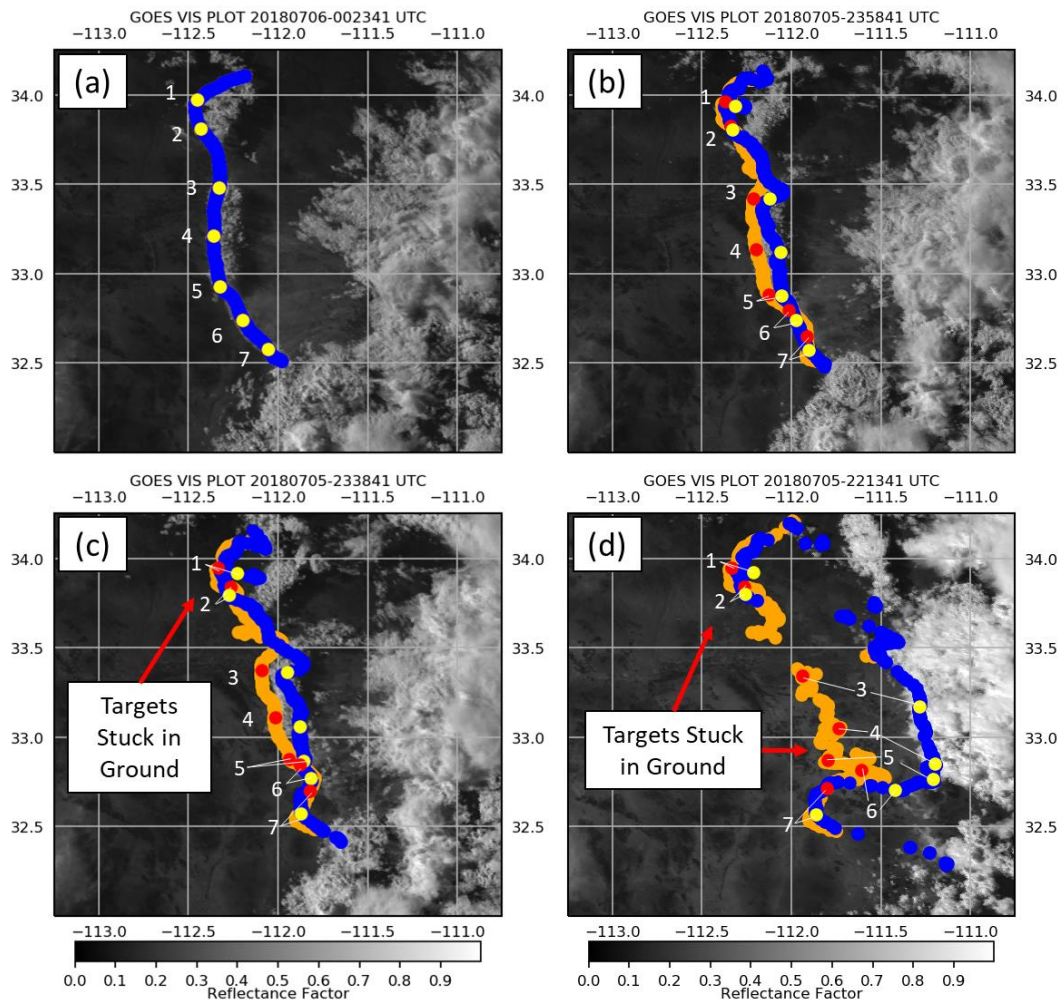


728

729 **Figure 8.** GOES-16 0.64- $\mu$ m visible channel imagery on 5 July 2018 at a) 2258 UTC, b) 2338  
730 UTC, c) 2358 UTC, and d) 0023 UTC over central Arizona shown with every 20<sup>th</sup> optical flow  
731 vector in the x and y directions (subsampled for image clarity) illustrated with yellow wind bars  
732 (knots). Circles represent motion < 5 kts, which commonly occur over ground pixels.

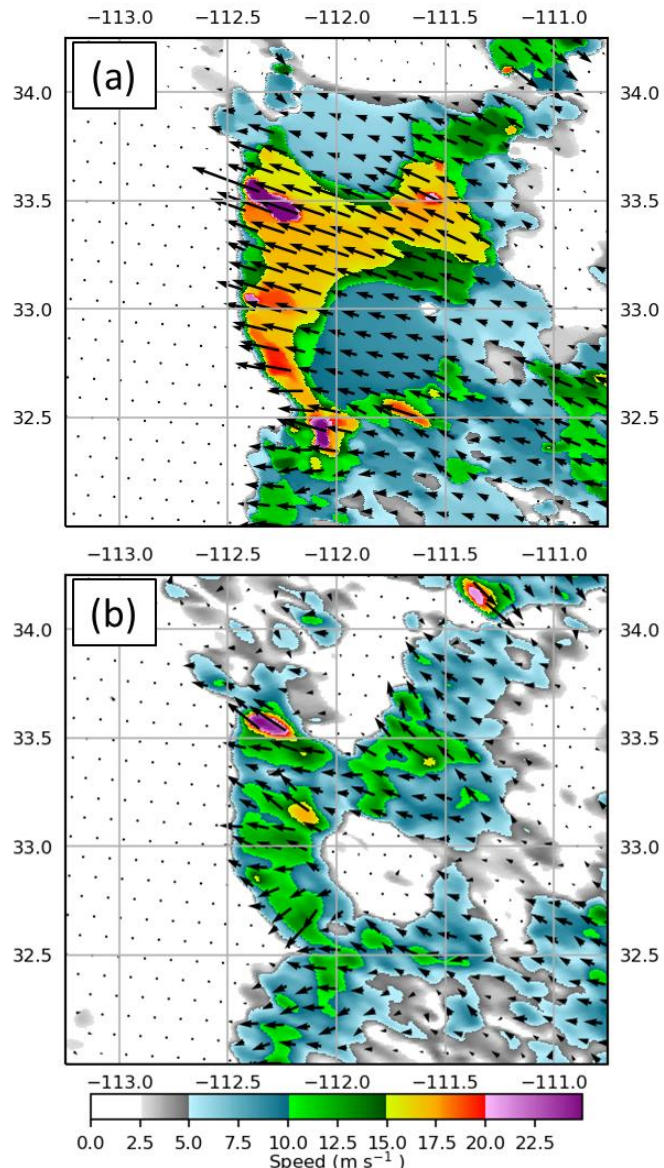
733

734



735

736 **Figure 9.** The GOES-16 0.64- $\mu$ m visible imagery shown with image targets backtracked from  
737 subjective identification in Fig. 7a at 0023 UTC 6 July 2018 using the B04 method (blue/yellow)  
738 and the Wu et al. (2016) approach (orange/red) at a) 0023 UTC, b) 2358 UTC, c) 2338 UTC and  
739 d) 2213 UTC. Individual points are highlighted from each approach (yellow and red dots; see  
740 text).  
741



742

743 **Figure 10.** Color shaded wind speed for 0023 UTC 6 July 2018 over central Arizona shown  
744 from a) the B04 optical flow method and b) the Wu et al. (2016) flow, shown with respective  
745 flow vectors and the subjective position of the front edge of the OFB (blue line).  
746